Roles for Arg426 and Trp111 in the Modulation of NADH Oxidase Activity of the Catalase-peroxidase KatG from *Burkholderia pseudomallei* Inferred from pH-Induced Structural Changes[†,‡]

Xavier Carpena,[#] Ben Wiseman,[§] Taweewat Deemagarn,[§] Beatriz Herguedas,[#] Anabella Ivancich,[||] Rahul Singh,[§] Peter C. Loewen,*[,§] and Ignacio Fita[#]

Departament de Biologia Estructural (IBMB-CSIC), Parc Científic de Barcelona, Josep Samitier 1-5, 08028 Barcelona, Spain, Department of Microbiology, University of Manitoba, Winnipeg, MB R3T 2N2 Canada, and Service de Bioénergétique, URA 2096 CNRS, Département de Biologie Joliot-Curie, CEA Saclay, 91191 Gif-sur-Yvette, France

Received January 4, 2006; Revised Manuscript Received February 28, 2006

ABSTRACT: Crystals of *Burkholderia pseudomallei* KatG retain their ability to diffract X-rays at high resolution after adjustment of the pH from 5.6 to 4.5, 6.5, 7.5, and 8.5, providing a unique view of the effect of pH on protein structure. One significant pH-sensitive change lies in the appearance of a perhydroxy group attached to the indole nitrogen of the active site Trp111 above pH 7, similar to a modification originally observed in the Ser324Thr variant of the enzyme at pH 5.6. The modification forms rapidly from molecular oxygen in the buffer with 100% occupancy after one minute of soaking of the crystal at room temperature and pH 8.5. The low temperature (4 K) ferric EPR spectra of the resting enzyme, being very sensitive to changes in the heme iron microenvironment, confirm the presence of the modification above pH 7 in native enzyme and variants lacking Arg426 or Met264 and its absence in variants lacking Trp111 or Tyr238. The indole-perhydroxy group is very likely the reactive intermediate of molecular oxygen in the NADH oxidase reaction, and Arg426 is required for its reduction. The second significant pH-sensitive change involves the buried side chain of Arg426 that changes from one predominant conformation at low pH to a second at high pH. The pH profiles of the peroxidase, catalase, and NADH oxidase reactions can be correlated with the distribution of Arg426 conformations. Other pH-induced structural changes include a number of surface-situated side chains, but there is only one change involving a displacement of main chain atoms triggered by the protonation of His53 in a deep pocket in the vicinity of the molecular 2-fold axis.

The first example of a catalase-peroxidase was identified (*1*) and sequenced (*2*) in *Escherichia coli* where the name KatG[1] was assigned (*3*). The enzyme has since been characterized in many other bacteria, archaebacteria, and a few fungi (*4*). While originally named for its obvious bifunctionality with catalase and general peroxidase activities, more recent work has shown that some examples of the enzyme also have associated NADH oxidase, INH lyase, and isonicotinoyl-NAD synthase activities (*5*). The latter two activities are responsible for the activation of isoniazid as an anti-tubercular drug in *Mycobacterium tuberculosis* (*6*−*10*), a cause for considerable interest in the enzyme.

Catalase-peroxidases are most commonly isolated as homodimers with each subunit having two distinct but sequence-related domains. The domains are also related to the single domain of peroxidases from higher organisms both in sequence and structure. It is conjectured that the two-domain structure of KatGs evolved in a gene duplication and fusion event (*11*) and then subsequently evolved back to the single-domain peroxidase found in eukaryotes (*4*). The unique structural features responsible for imparting catalase activity to the core of KatG, which is essentially a peroxidase, were lost during this subsequent evolution.

The catalase and peroxidase reactions both involve compound I formation (reaction 1), with the heme initially oxidized to the oxoferryl state (Fe^{IV}═O) and a porphyrin cation π-radical ($Por^{\circ+}$) and subsequently undergoing intramolecular electron transfer to form protein-based radical intermediates in some enzymes. In particular, the formation of a [$Por^{\circ+}$−Fe^{IV}═O] intermediate in *Synechocystis* PCC6803 KatG is followed by tryptophanyl and tyrosyl radical intermediates in the absence of reducing substrate (reaction 2) (*12*). It is in the reduction of compound I back to resting

[†] This work was supported by a grant OGP9600 from the Natural Sciences and Engineering Research Council of Canada (to P.C.L.), by the Canadian Research Chair Program (to P.C.L.) and by fellowship EX-2003-0866 from the Ministerio de Educación Cultura y Deporte, Spain (to X.C.).

[‡] Structure factors and coordinates have been submitted to the Protein Data Bank under accession numbers 2FXG (pH 4.5 structure), 2FXH (pH 6.5 structure) and 2FXJ (pH 8.5 structure).

* To whom correspondence should be addressed. Phone: (204) 474-8334; fax: (204) 474-7603; e-mail: ploewen@cc.umanitoba.ca.

[#] Departament de Biologia Estructural (IBMB-CSIC), Parc Científic de Barcelona.

[§] University of Manitoba.

[||] Service de Bioénergétique, URA 2096 CNRS.

[1] Abbreviations: BpKatG, *Burkholderia pseudomallei* KatG; HmKatG, *Haloarcula marismortui* KatG; MtKatG, *Mycobacterium tuberculosis* KatG.; EcKatG, *Escherichia coli* KatG; SyKatG, *Synechocystis* PCC6803 KatG; rmsd, root-mean-squared deviation; EPR, electron paramagnetic resonance; PEG, poly(ethylene glycol); MPD, 2-methyl-2,4-pentanediol.

10.1021/bi060017f CCC: $33.50
Published on Web 03/30/2006

state that catalases and peroxidases differ. In catalases, compound I is reduced in a single two-electron transfer from H_2O_2 (reaction 3), whereas peroxidases undergo two sequential one-electron transfers, usually from organic donors, and involve an intermediate called compound II (reactions 4 and 5).

$$\text{Enz (Por}-\text{Fe}^{\text{III}}) + H_2O_2 \rightarrow \text{Cpd I (Por}^{\circ+}-\text{Fe}^{\text{IV}}=\text{O}) + H_2O \quad (1)$$

$$\text{Cpd I (Por}^{\circ+}-\text{Fe}^{\text{IV}}=\text{O}) \rightarrow \text{CpdI (Por}-\text{Fe}^{\text{IV}}-\text{OH Trp}^{\circ}) \rightarrow \text{CpdI (Por}-\text{Fe}^{\text{IV}}-\text{OH Tyr}^{\circ}) \quad (2)$$

$$\text{Cpd I (Por}^{\circ+}-\text{Fe}^{\text{IV}}=\text{O}) + H_2O_2 \rightarrow \text{Enz (Por}-\text{Fe}^{\text{III}}) + H_2O + O_2 \quad (3)$$

$$\text{Cpd I (Por}^{\circ+}/\text{Trp}^{\circ}/\text{Tyr}^{\circ}-\text{Fe}^{\text{IV}}-\text{OH}) + AH \rightarrow \text{CpdII (Por}-\text{Fe}^{\text{IV}}-\text{OH}) + A_{ox} \quad (4)$$

$$\text{CpdII (Por}-\text{Fe}^{\text{IV}}-\text{OH}) + AH \rightarrow \text{Enz (Por}-\text{Fe}^{\text{III}}) + H_2O + A_{ox} \quad (5)$$

While NADH can serve as the electron donor in the peroxidase reaction in KatGs (reactions 4 and 5), it is also a substrate for an oxidase reaction in BpKatG in which electrons are transferred to molecular oxygen generating H_2O_2 between pH 6 and 8 (reaction 6) and superoxide ion between pH 8 and 10 (reaction 7) (*5*).

$$NADH + H^+ + O_2 \rightarrow NAD^+ + H_2O_2 \quad (6)$$

$$NADH + 2O_2 \rightarrow NAD^+ + 2O_2^- + H^+ \quad (7)$$

Detailed structural information of KatGs is available from the crystal structures of the enzymes from *Haloarcula marismortui*, HmKatG (*13*, *14*), *Burkholderia pseudomallei*, BpKatG (*15*, *16*), *Synecococcus* sp. (*17*), and *Mycobacterium tuberculosis*, MtKatG (*18*). These structures in combination with the biochemical characterization of variants of EcKatG (*E. coli* KatG), SyKatG (*Synechocystis* KatG), and BpKatG, lead to the identification of a number of catalase-specific residues, including the cross-linked adduct of Trp111, Tyr238, and Met264, unique to KatGs, and Arg426, Asp141, and Asn142 (all numbering is for BpKatG unless otherwise stated) (*5*, *19*−*25*). His112 in the distal heme pocket is required for both catalase and peroxidase reactions. Finally, Arg108, also in the distal heme pocket, is usually considered to be essential at least for the peroxidase reaction, but its removal only slightly lowers catalase and peroxidase activities provided Trp111 is present, suggesting that Trp111 can effectively replace Arg108 in both compound I formation and reduction.

Of these catalase-specific residues, Arg426 is unique in occupying two conformations, the relative proportions of which vary among the different crystal structures. In one position, the guanidinium group forms an ionic association with Tyr238 in the Trp-Tyr-Met adduct (conformation Y), and in the second position, it is shifted to a region containing two other arginine residues (conformation R). The proportion of conformation Y varies from about 0% in MtKatG (*18*), to 30% in BpKatG (*16*), to 80% in SyKatG (*17*, *26*) and 100% in HmKatG (*14*), presenting a striking correlation with the pH values of crystallization, pH 4.5 for MtKatG, pH 5.6 for BpKatG, pH 6.3 for SyKatG, and pH 8.1 for HmKatG. The apparent correlation between the conformation of Arg426 and the pH of crystallization was tentatively confirmed by increasing the pH of a crystal of BpKatG to 8.0 causing an increase in the amount of conformation Y to about 100% (*26*).

The apparently facile movement of the side chain of Arg426 coupled with its key role in catalase activity suggested that it can act as a molecular switch reversibly interacting with the Trp-Tyr-Met adduct to inductively alter heme reactivity. The correlation between the pH sensitivity of the Arg426 conformation and its role as a molecular switch of enzyme reactivity presented an unusual phenomenon that warranted further investigation. In this report, a systematic study of changes occurring in the structure of BpKatG as the pH of crystals is varied across the pH range from 4.5 to 8.5 is reported. In addition to movement of some side chains including that of Arg426, the active site Trp111 is shown to suffer rapid oxidation above pH 7. EPR spectroscopy confirms the presence of the Trp modification in some variants and not in others, suggesting its role as an intermediate in the NADH oxidase reaction.

MATERIALS AND METHODS

Variants of BpKatG were prepared as described previously using oligonucleotide primers with appropriate sequences (*27*) and, along with native BpKatG, were purified from the catalase-deficient *E. coli* strain UM262 and crystallized as previously described (*15*, *16*). For pH change, crystals were soaked for 1 min in 20% PEG 4K, 20% MPD, and 100 mM of the appropriate buffer, that is, sodium acetate pH 4.5 or 100 mM Tris-HCl at pH 6.5, 7.5, or 8.5 before flash cooling for data collection. Attempts to generate an oxoferryl species at pH 7.5 involved soaking the crystal for 1 min in 20% PEG 4K, 20% MPD, and 100 mM Tris-HCl pH 7.5 and then soaking with 1 mM peroxyacetic acid in the same pH 7.5 Tris buffer for 1 min, followed by flash cooling and data collection. Diffraction data were obtained from crystals cooled with a nitrogen cryo-stream. As before, crystals were primitive orthorhombic space group $P2_12_12_1$ with one dimeric molecule in the crystal asymmetric unit. The diffraction data sets were processed using the program DENZO and scaled with program SCALEPACK (*28*). 5% of the measured reflections in every data set were reserved for R_{free} monitoring during automatic refinement (Table 1). The resulting map showed clear continuity over the complete length of BpKatG from Asn35 to Ala748 in both subunits. Refinement was completed using the program REFMAC (*29*) and the graphics program O (*30*). All figures were prepared using SETOR (*31*).

Low temperature (4 K) 9-GHz EPR measurements were performed using a Bruker ER 300 spectrometer with a standard TE_{102} cavity equipped with a liquid helium cryostat (Oxford Instrument) and a microwave frequency counter (Hewlett-Packard 5350B). Samples were prepared by buffer exchange using Centricon 10 microconcentrators (Amicon)

Table 1: Data Collection and Structural Refinement Statistics for BpKatG at pH 4.5, 6.5, 7.5, and 8.5[a]

	pH 4.5	pH 5.6	pH 6.5	pH 7.5	pH 8.5
Data Collection Statistics					
unit cell parameters					
space group	$P2_12_12_1$	$P2_12_12_1$	$P2_12_12_1$	$P2_12_12_1$	$P2_12_12_1$
a (Å)	101.0	100.7	100.5	100.3	100.4
b (Å)	114.9	113.5	114.8	114.9	114.9
c (Å)	174.7	174.8	174.6	174.9	174.0
α, *β*, *γ* (deg)	90, 90, 90	90, 90, 90	90, 90, 90	90, 90, 90	90, 90, 90
resolution (Å)	30−2.0 (2.07 2.00)	30−1.8 (1.92 1.85)	30−1.9 (1.97 1.90)	50−2.0 (2.10 2.05)	20−1.9 (2.00 1.95)
unique reflections	136981 (12282)	171198 (17006)	158979 (15673)	126202 (7891)	133778 (9181)
completeness (%)	98.6 (89.4)	99.6 (99.9)	99.8 (99.7)	99.2 (94.4)	91.2 (95.0)
R_{sym} (%)	7.5 (54.5)	8.3 (48.7)	7.5 (38.0)	11.6 (48.1)	9.9 (48.1)
$\langle I/\sigma I \rangle$	10.8 (1.9)	10.4 (3.2)	10.8 (5.6)	8.0 (2.2)	7.9 (2.4)
redundancy	3.6 (3.0)	4.4 (4.4)	7.4 (7.5)	4.4 (3.4)	4.8 (4.6)
Model Refinement Statistics					
resolution	20−2.0 (2.05 2.00)	20−1.9 (1.95 1.90)	20−1.9 (1.95 1.90)	20−2.0 (2.10 2.05)	20−1.9 (2.00 1.95)
no. of reflections	128885 (8418)	149135 (10,868)	150790 (10,947)	119528 (8168)	126909 (9,518)
free reflections	6790 (458)	7796 (555)	7888 (558)	6350 (461)	6673 (488)
R_{cryst} (%)	15.7 (23.4)	18.2 (26.1)	14.3 (17.0)	14.6 (20.4)	15.0 (20.4)
R_{free} (%)	20.6 (29.5)	22.4 (33.3)	17.9 (24.0)	19.5 (30.9)	19.7 (28.5)
no. residues	1428	1428	1428	1428	1428
no. waters	1386	1506	1516	1527	1537
average B-factor (Å^2)					
protein	33.01	16.96	27.30	21.78	17.13
water	36.27	21.66	32.77	26.04	22.62
all atoms	33.30	18.51	27.91	22.26	17.78
rms deviations					
bond lengths (Å)	0.04	0.02	0.03	0.03	0.03
bond angles (deg)	2.76	1.62	2.01	2.32	2.26

[a] Values in parentheses correspond to the highest resolution shell.

and 20 mM TRIS-maleate buffer for pH 5.5, 6.4, 7.6, and 8.4 or 20 mM succinate buffer for pH 4.3. EPR samples were measured as frozen solutions in 4-mm quartz tubes.

Catalase activity was determined by the method of Rorth and Jensen (*32*) in a Gilson oxygraph equipped with a Clark electrode. One unit of catalase is defined as the amount that decomposes 1 μmol of H_2O_2 in 1 min in a 60 mM H_2O_2 solution at pH 7.0 at 37 °C. Peroxidase activity was determined using 2,2′-azinobis(3-ethylbenzothiazolinesulfonic acid) (ABTS) (*33*). One unit of peroxidase is defined as the amount that decomposes 1 μmol of ABTS in 1 min in a solution of 0.3 mM ABTS ($\epsilon = 36\,800$ M^{-1} cm^{-1}) and 2.5 mM H_2O_2 at pH 4.5 and 25 °C. Free radical production for NADH oxidase determination at 540 nm was assayed by NBT (nitroblue tetrazolium) reduction to a monoformazan ($\epsilon = 15\,000$ M^{-1} cm^{-1}). NADH oxidase activity was also determined spectrophotometrically at 340 nm using $\epsilon = 6300$ M^{-1} cm^{-1} for NADH. One unit of NADH oxidase is defined as the amount that produces 1 nmol of radical or that decomposes 1 nmol of NADH in a solution of 250 μM NADH at 25 °C at pH 8.75. Protein was estimated according to the methods outlined by Layne (*34*).

RESULTS

Changes in pH Affect the Structure of BpKatG. In the four KatGs so far crystallized, the equivalent of BpKatG Arg426 adopts two conformations, the relative amounts of which vary, seemingly as a function of the pH of crystallization (*26*). The effect of pH change on the structure of BpKatG was therefore investigated by soaking crystals originally grown at pH 5.6 at pH 4.5, 6.5, 7.5, and 8.5 prior to X-ray diffraction data collection (Table 1). In all cases, the electron density maps defined main chain and side chain atoms of 1426 amino acids, two metal ions, two heme groups, and a variable number of waters in two subunits. As in the original BpKatG structure obtained at pH 5.6, the 34 N-terminal residues are not visible, but the maps show clear continuity

Table 2: Summary of pH Induced Changes in the Structure of BpKatG

	pH 4.5	pH 5.6	pH 6.5	pH 7.5	pH 8.5
(a) Changes in the Vicinity of Arg426					
Thr119	70:30	70:30	50:50	25:75	100
Arg426 (R:Y)	>90:<10	70:30	50:50	25:75	<5:>95
W−OOH[a]	0	0	0	75	100
(b) Changes in the Core Near the 2-Fold Axis					
His53	100A	100B	100B	100B	100B
His55	100A	100B	100B	100B	100B
Glu198	50:50	100B	100B	100B	100B
(c) Other Changes					
Arg255	100A	100A	70:30	50:50	50:50
Arg403	50:50	100A	100A	100A	100A
Thr571	70:30	50:50	30:70	100B	100B
Glu589	100A	100A	100A	70:30	50:50
Arg610	100A	100A	100A	100B	100B
Gln647	30:70	100B	100B	100B	100B
Glu657	100A	100A	100A	70:30	50:50
(d) Residues Adopting Two Conformations That Do Not Change					
Val633	50:50	50:50	50:50	50:50	50:50
Gln711	50:50	50:50	50:50	50:50	50:50

[a] W−OOH is the perhydroxy modification on the indole nitrogen of W111.

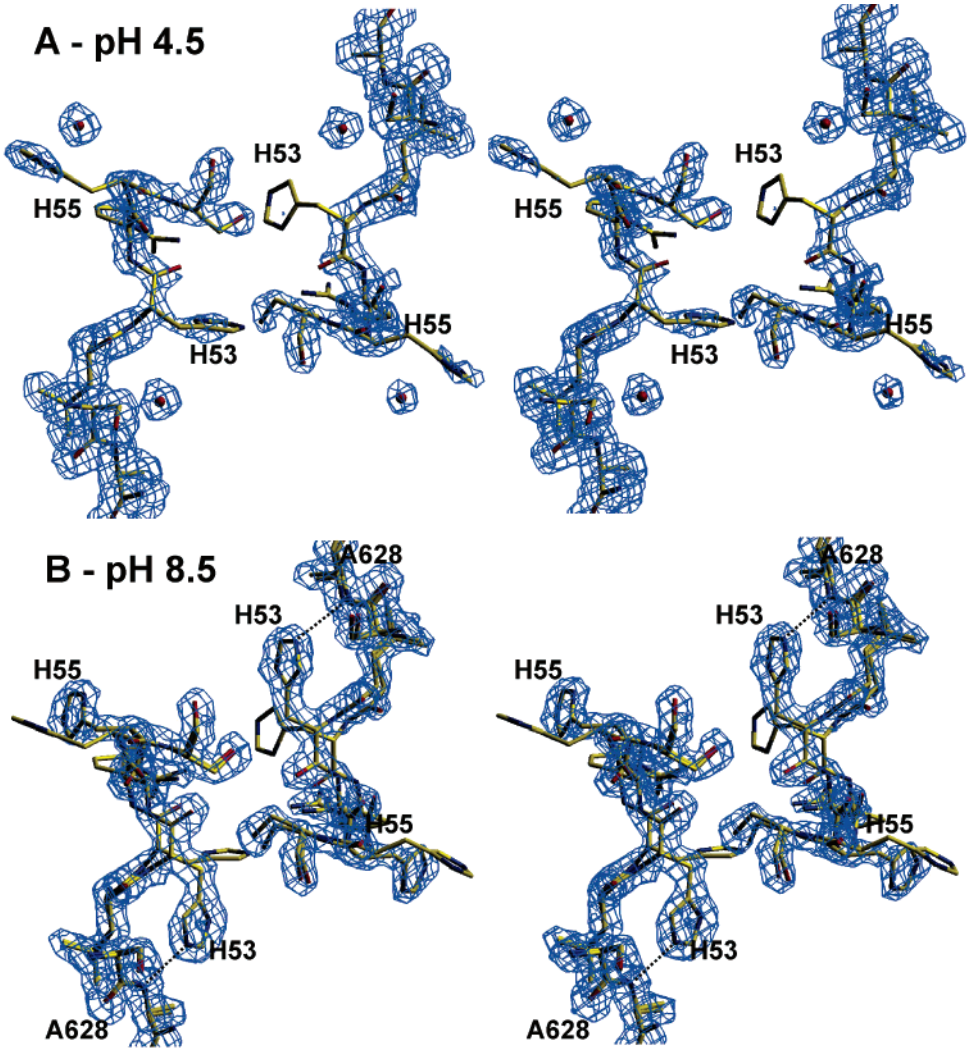

FIGURE 1: Changes in the conformation of His53 and His55 and the associated main chain atoms with pH. (A) The $2F_o - F_c$ electron density map at $\sigma = 1.0$ from the crystal at pH 4.5 is shown with the model superimposed. (B) The $2F_o - F_c$ electron density map at $\sigma = 1.0$ from the crystal at pH 8.5 with the models from both pH 8.5 and pH 4.5 superimposed to show the significant changes in location of the side chains of His 53 and His55. The association between His53 and the main chain nitrogen of Ala628 at pH 8.5, which is broken as a result of protonation of the imidazole ring at pH 4.5, is shown with a dashed line.

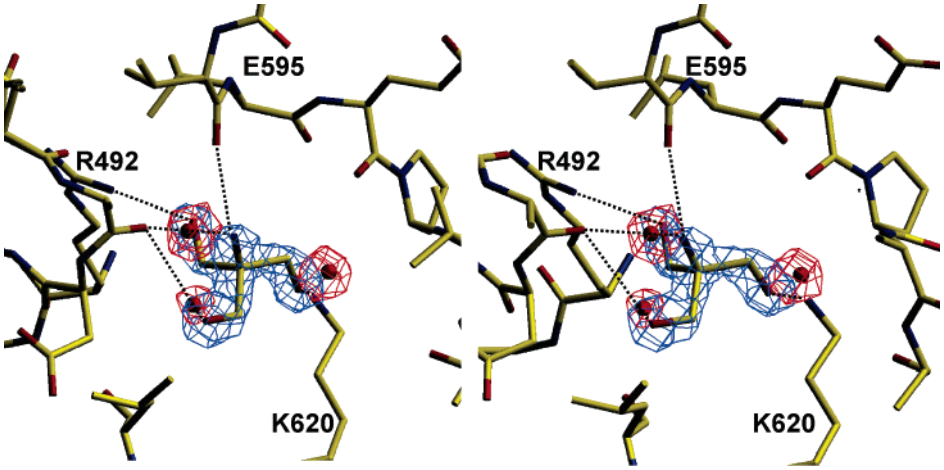

FIGURE 2: Stereoview of the environment surrounding the Tris binding site. The $2F_o - F_c$ electron density map drawn at $\sigma = 1.0$ corresponding to the three waters in the crystal at pH 4.5 is shown in red. The $2F_o - F_c$ electron density map drawn at $\sigma = 1.0$ corresponding to the Tris molecule in the crystal at pH 8.5 is shown in blue. Of particular interest is the hydrogen bond with Arg492 which is situated close to Arg426 in the R conformation.

from Asn35 to Ala748 in two subunits. All soaked crystals diffracted to 2.0 Å or better, very similar to the original crystals at pH 5.6.

Comparison of the structures reveals remarkably few changes, which is evident in the extremely small average 0.3 Å rmsd in main chain atom location between pH 4.5

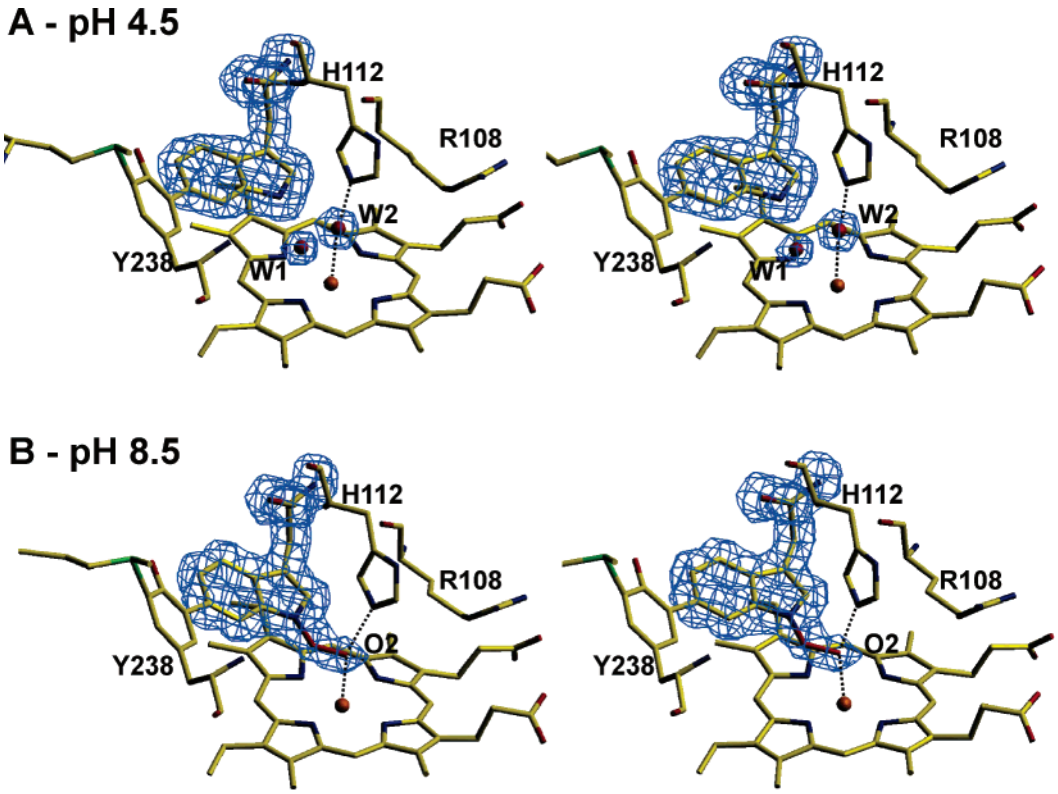

FIGURE 3: Stereo diagrams showing the appearance of a covalent modification on the indole nitrogen of Trp111 with pH. In A, at pH 4.5 there is <10% occupancy of the modification on the indole nitrogen of Trp111 and two waters are closely associated in the heme cavity. The $2F_o - F_c$ electron density map is drawn at $\sigma = 1.0$. The distances between water W2 and the heme iron and imidazole of His112 are 2.8 and 2.7 Å, respectively. In B, at pH 8.5, the $2F_o - F_c$ electron density map at $\sigma = 1.0$ is consistent with a perhydroxy modification covalently attached to the indole nitrogen and waters W1 and W2 are displaced. The distances between O2 of the perhydroxy modification and the heme iron and imidazole of His112 are 2.8 and 2.9 Å respectively. In the second subunit, a small amount of the water #1 is retained.

Table 3: Comparison of the Catalase, Peroxidase, and Oxidase Activities in BpKatG at Different pHs and the Arg426 Variants at the Optimum pH[a] for Each Reaction

	catalase	peroxidase	oxidase$_{(340)}$	oxidase$_{(560)}$
		units/mg		
BpKatG				
pH 4.5	2021 ± 140	8.9 ± 0.2	0.2 ± 0.03	nd[b]
pH 5.6	3010 ± 210	1.6 ± 0.07	0.5 ± 0.07	nd
pH 6.5	4300 ± 300	0.6 ± 0.04	1.9 ± 0.3	nd
pH 7.5	2020 ± 140	nd	4.3 ± 0.6	0.7 ± 0.1
pH 8.5	560 ± 39	nd	6.6 ± 0.6	7.1 ± 1.1
R426A	95 ± 9.0	10.8 ± 1.4	0.57 ± 0.19	0.16 ± 0.03
R426E	110 ± 5.0	10.3 ± 0.8	0.54 ± 0.18	0.25 ± 0.01
R426L	110 ± 4.0	11.0 ± 2.4	0.74 ± 0.01	0.06 ± 0.01
R426K	3000 ± 250	10.6 ± 0.4	0.37 ± 0.01	0.16 ± 0.03

[a] The optimum pHs were catalase pH 7.0, peroxidase pH 4.5, oxidase (both) pH 8.75. [b] nd, not detectable.

and 8.5, and the fact that only 10 (including the poorly defined Lys64 and Arg161 not listed in Table 2) of 713 side chains exhibit rmsd's greater than 2 Å. Such limited changes in protein structure across a span of 4 pH units, despite the ionization of histidines and possibly a few other residues with unique microenvironments such as Tyr238, provides a unique view of the inherent stability in a protein structure. In BpKatG there is only one significant main chain distortion (rmsd greater than 1Å) in the region of residues 52−55 that is triggered by a change in protonation of His53 (Figure 1). The conserved His53, when unprotonated, forms a hydrogen bond with the main chain nitrogen of Ala628, and this is disrupted by protonation. As in the structure of Ser324Thr variant (*35*), the perhydroxy modification on the heme found in the first BpKatG structure determined (*16*) was absent from all of the structures presented here. This would seem to be the result of batch specific variation, but the cause is not understood.

Among the other catalogued changes (Table 2), there are two that are significant because they have mechanistic implications. One is the appearance at high pH of a covalent modification on the indole N of Trp111 in the heme cavity similar to a modification originally observed in the structure of the Ser324Thr variant of BpKatG (*35*). The second is the gradual change in conformation of Arg426 from predominantly conformation R at pH 4.5 to predominantly conformation Y at pH 8.5. In addition to these structural changes, the models at pH 6.5, 7.5, and 8.5 also contain one very well defined molecule of Tris, used in the buffers to change the pH, bound to each subunit (Figure 2), and the models at pH

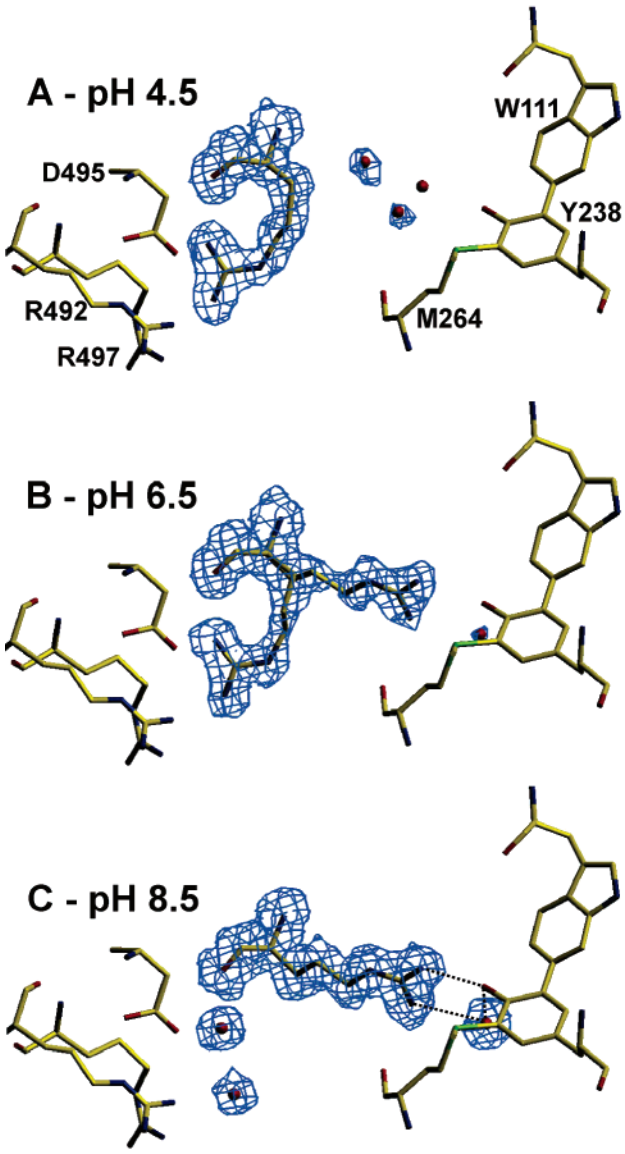

FIGURE 4: Change in the conformation of Arg426 with pH. The $2F_o - F_c$ electron density maps at $\sigma = 1.0$ corresponding to Arg426 in crystals changed to pH 4.5 (A), pH 6.5 (B), and pH 8.5 (C). In A >90% of Arg426 is in conformation R in close proximity to Arg492, Arg497, and Asp495. At pH 8.5, Arg426 is >90% in conformation Y associated with Tyr238. At pH 6.5, there is approximately a 50:50 mixture of conformations R and Y.

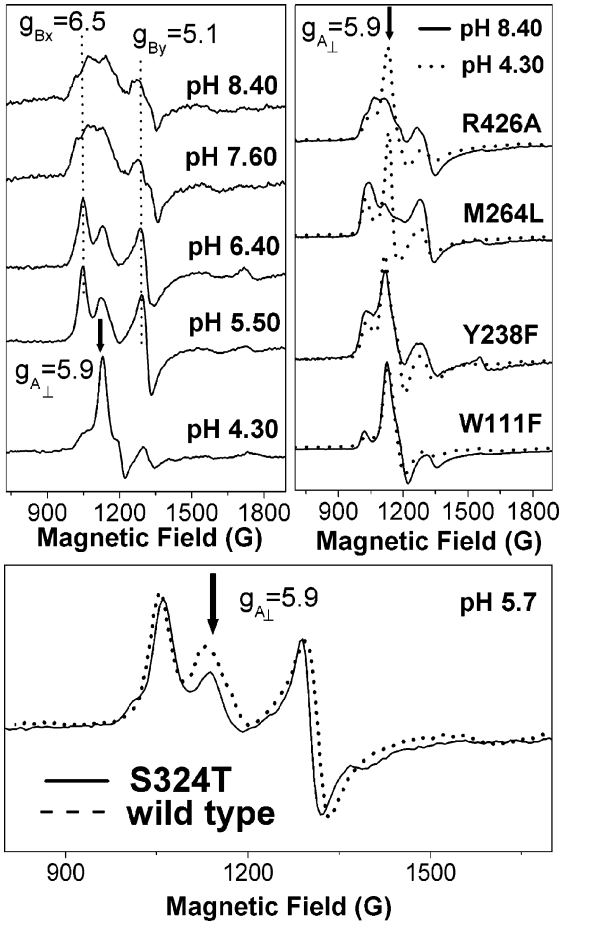

FIGURE 5: The 9-GHz EPR spectra of wild-type (left panel) and distal side variants (right panel) of *B. pseudomallei* catalase-peroxidase in the resting (ferric) state and as a function of pH. Only the expansion of the $g \approx 6$ region of the spectra is shown for clarity. The axial (arrow) and the rhombically distorted (vertical dotted lines) signals contributing to the spectra are shown. The comparison of the ferric signal of the S324T variant and the wild-type enzyme is shown in the bottom panel. All spectra were recorded at 4 K, 5G modulation amplitude, 1 mW microwave power, 100 kHz modulation frequency.

6.5 and 7.5 both contain a second Tris with a slightly lower occupancy. Given the lack of success in demonstrating substrate binding to a KatG, particularly of INH, it is heartening that Tris presents as the first ligand to have its binding demonstrated.

Perhydroxy Modification on the Indole of Trp111. A major pH-related change in the structure of BpKatG lies in the modification of the Trp111 indole in the heme cavity (Figure 3; Table 2). At pH 4.5, no extraneous electron density is evident in the vicinity of the indole N except for two nearby waters, W1 and W2, 2.8 and 2.6 Å away (Figure 3). However, as the pH is increased from 5.6 to 8.5, electron density adjacent to the indole N increases, suggesting the gradual appearance of a modification from a small amount (~5 to 10% occupancy) to 100% occupancy. (Figure 3, Table 2). The electron density at pH 7.5 suggests a modification similar to that previously observed in the S324T variant of BpKatG (*35*), ascribed to a perhydroxy group with the O-2 atom adopting two different conformations, displacing either water 1 or water 2 depending on the conformation. The electron density in one subunit at pH 8.5 is different in that it suggests a perhydroxy group adopting one conformation with O-2 situated 2.7 Å from the heme iron and both waters 1 and 2 absent (Figure 3). Because there is no reason to expect a pH dependence in the conformation of the perhydroxy modification, it is likely that the perhydroxy modification in crystals at pH 8.5 and 7.5 and the S324T variant actually occupies only one conformation, and water 2 is present in varying amounts associated with O-1, to give the appearance of two conformations. Crucially, the pH-dependent EPR spectrum correlates with the presence of the Trp modification at pH ≥ 7.0 (see below).

The effect of the indole modification on oxoferryl formation to compound I was investigated by attempting to form the oxoferryl intermediate at pH 7.5 when there is about 70% occupancy of the indole modification. Unlike oxoferryl formation at pH 5.6 which proceeded rapidly (*26*), the attempts at pH 7.5 did not yield a definitive oxoferryl species and did not increase the amount of R conformation Arg426

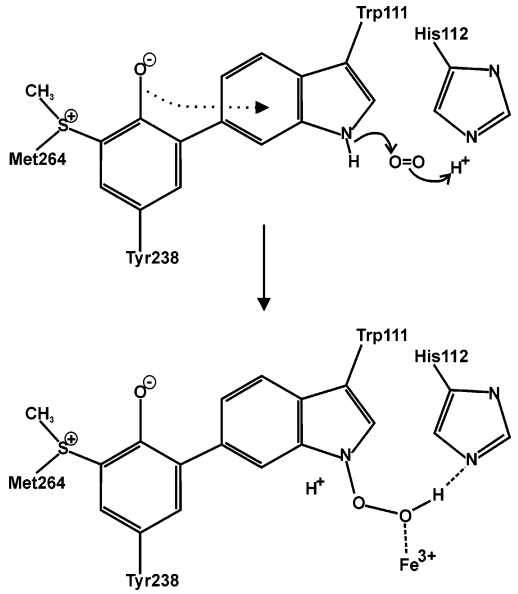

FIGURE 6: Scheme showing a possible mechanism for the oxidation of the indole nitrogen of Trp111. The dotted arrow in the top panel is intended to demonstrate electron flux from the tyrosinate ion toward the indole. The dashed lines in the lower panel denote associations of the O2−H of the perhydroxy with the heme iron (2.7 Å) and the His112 imidazole (2.9 Å).

(data not shown). Thus, there is a correlation between the lack of oxoferryl formation and the presence of the perhydroxy modification on the indole, but this cannot be separated from the alternate explanations that increased Arg426-Tyr238 association at the higher pH interferes with oxoferryl formation (26) or that oxoferryl formation is slower at higher pH.

Influence of Arg426 Movement on Enzymatic Activity. The gradual change in the location of Arg426 with pH ranges from about 10% conformation Y at pH 4.5 to >95% at pH 8.5, with intermediate amounts of 30, 50, and 75% at pH 5.6, 6.5, and 7.5, respectively (Figure 4; Table 2). The relative amounts of Y and R conformations at different pHs are also correlated with the relative amounts of the two rotamers of Thr119 and the occupancies of several water molecules, located in the vicinity of the guanidinium group of Arg426 in the R conformation (Table 2). These correlated changes emphasize that a number of interactions, besides the dominant association between Arg426 and Tyr238, contribute to the relative stability of the Y and R conformations.

The catalase and NADH oxidase reactions are similar in that there is an initial oxidation step (the heme to compound I in catalase and Trp111 to indole-perhydroxy in oxidase) followed by a reduction step (compound I to water in catalase and indole-perhydroxy to superoxide in oxidase). Given the importance of the Met-Tyr-Trp adduct to both reactions, it was anticipated that Arg426 might have a role in modulating the oxidase reaction as well as the catalase reaction. This is clearly evident in variants lacking Arg426 that all exhibit significantly lower NADH oxidase, reflecting their lower catalase activities (Table 3).

pH-Induced Changes Detected by 9 GHz EPR Spectroscopy. EPR spectroscopy, performed at liquid helium temperatures on frozen solution samples was used as a complementary approach to monitor the pH-induced changes in the heme active site of BpKatG. The high sensitivity of the EPR spectrum to subtle modifications in the heme environment induced by distal and proximal side mutations has proved to be an important tool to better understand changes in the activity of SyKatG (*12*). The low temperature (4 K) 9 GHz-EPR spectrum of resting BpKatG is characteristic of high-spin ($S = 5/2$) pentacoordinated ferric heme enzymes, with two main resonances at $g \approx 6$ and $g \approx 2$. Specifically, the EPR spectrum of the resting enzyme shows the contribution of two predominant forms (Figure 5, left panel): a rhombically distorted signal, with $g_{Bx} = 6.50$, $g_{By} = 5.10$ and $g_{Bz} = 1.97$ and an axial signal, with $g_{A\perp} = 5.90$ and $g_{All} = 1.99$. As previously shown for SyKatG (see Figure 1 in ref 12), the relative contribution of each signal to the EPR spectrum of BpKatG is pH-dependent, with the axial signal becoming predominant at acidic pH (see arrow in Figure 5, left panel). Interestingly, the comparison of the previously characterized pH-dependent EPR spectra of SyKatG to that of BpKatG show a similar trend of the relative contributions of the axial and rhombically distorted signals in both enzymes below pH 7. In the spectra at pH 7.3 and 8.3, the axial signal becomes predominant for SyKatG, whereas for BpKatG the relative contribution of the axial signal is rather low (Figure 5, left panel). Residues in the heme active sites of KatG's are highly conserved making an enzyme-specific difference in protonation unlikely. Therefore, the differences observed in the EPR spectra of BpKatG at pH ≥ 7 as compared to SyKatG must be the result of some other change in the interactions of the heme iron with its microenvironment. The EPR spectrum (g tensor) is highly sensitive to small differences in relative positioning of the iron, the water(s) and the imidazole or indole nitrogens; the perhydroxy modification on Trp111 with its reorganized water matrix in the heme cavity presents an obvious explanation. Consequently, the resulting subtle changes in relative distances and/or hydrogen bonding strengths in the heme iron environment induced by the perhydroxy modification on Trp111 observed in the crystal structure are significant enough to modify the ferric EPR spectrum. The absence of the indole modification predicted by the EPR spectrum of SyKatG and the correlation of the modification with the NADH oxidase activity suggests that SyKatG should exhibit very low NADH oxidase levels, and this is indeed the case (data not shown).

The EPR spectra of three distal side variants affecting Trp111 to different extents (W111F, Y238F, and M264L) are also consistent with the influence of the perhydroxy modification on the BpKatG EPR spectrum. The EPR spectrum of the M264L variant, where the cross-link between Trp111 and Tyr238 is present (*23*) and no significant geometry change on the microenvironment of the iron is expected, is very similar to that of native BpKatG at pH 8.4 (Figure 5, right panel), with a predominant rhombically distorted signal. In contrast, the EPR spectra of both W111F and Y238F at pH 8.4 have a predominant axial signal (Figure 5, right panel), indicative of differences in the microenvironment of the heme iron which can be rationalized by the absence of the perhydroxy modification either because tryptophan is absent (W111F) or not cross-linked to Tyr238 (Y238F). This is also consistent with the absence of oxidase activity in both variants (*5*, *26*). In particular, the EPR spectra of the Arg426 variants, represented by R426A (the spectra of R426K and R426I are identical) in Figure 5 (right panel),

are indistinguishable from the native BpKatG spectra over the whole pH range, suggesting the presence of the perhydroxy modification despite the lack of oxidase activity.

The perhydroxy-indole modification was originally observed in the structure of the S324T variant at pH 5.6 (*35*), whereas no such modification is evident in the structure of the native enzyme at the same pH. Significantly, the ferric EPR spectrum of the S324T variant at pH 5.7 clearly shows a lower contribution of the axial signal ($g_{A\perp} = 5.90$ and $g_{All} = 1.99$) as compared to the native enzyme at the same pH (Figure 5, bottom panel) that could be explained by the presence of the perhydroxy-indole modification on Trp111. The small difference in the g values of the rhombically distorted signal of the S324T variant ($g_{Bx} = 6.36$, $g_{By} = 5.17$ and $g_{Bz} = 1.97$) as compared to the native enzyme can be accounted for by the geometrical changes induced by the hydrogen bonding of the introduced Thr residue with the heme propionates (*35*).

DISCUSSION

The appearance of a perhydroxy modification on the indole nitrogen of Trp111, situated on the distal side of the heme, is one of two significant pH-induced changes observed in BpKatG. The rapidity of perhydroxy-indole formation, 100% yield after just 1 min soaking of the crystal at pH 8.5, suggests a very facile reaction with molecular oxygen in the buffer at high pH, which correlates well with the pH optimum of 8.75 for the NADH oxidase reaction (*5*). The covalent attachment of oxygen to the indole creates a very different molecular species compared to its noncovalent binding to heme iron in other oxygen binding proteins (Figure 6). The fact that NADH is too large to fit into the heme cavity necessitates electron transfer from a remotely bound NADH to the oxygen most likely through the protein, and covalent linkage of the oxygen to the indole makes possible direct electron transfer from the protein. It is also important that the perhydroxy-indole modification was detected by both X-ray crystallography and EPR spectroscopy, because it suggests that the modification forms in aqueous solution upon buffer exchange prior to freezing the solution samples for EPR measurements. This is consistent with the previous evidence that frozen solution samples of CcP used for the EPR measurements mimic very well the geometry of the heme active site revealed by the crystal structure of the enzyme (*36*, *37*).

The perhydroxy modification was first observed in the S324T variant of Bp*K*atG at pH 5.6, accompanied by 70% conformation Y as compared to 30% in the native enzyme at that pH (*35*). At the time, the significance of the indole modification and conformational change of Arg426 in the S324T variant were not obvious, and no attempt was made to provide an explanation. Subsequently, the EPR spectrum of the S324T variant at pH 5.7 has been found to be consistent with the presence of the modification. The additional Thr324 methyl group must facilitate indole oxidation and influence the Arg426 conformation, as well as constrict the heme access channel interfering with INH activation. The significance of W111 indole reactivity being modified by such a subtle and remote structural change lies in the context of the other unusual reactions in the BpKatG active site, including the perhydroxy-heme modification present in some batches of protein and the cross linked Met-Tyr-Trp adduct.

The formation of the perhydroxy-indole modification appears to be correlated with the movement of Arg426 from R to Y conformation. However, the independence of the two processes is demonstrated by the EPR spectra of the R426 variants being consistent with the presence of the modification at pH>7 despite the absence of Arg426. There is, however, a clear requirement for Arg426 in the oxidase reaction (Table 3) implying that, if Arg426 is not required for perhydroxy-indole formation, it must be required for perhydroxy-indole reduction. Furthermore, because Arg426 is in conformation Y at pH 8.5, its role is similar to that in the catalase reaction, inductively lowering electron density on the indole and facilitating the reduction reaction.

The second pH-induced change in structure is the shift in equilibrium between conformations R and Y of Arg426, which can be correlated with and explain, at least in part, the pH optima for the peroxidase, catalase, and NADH oxidase reactions of 4.5, 6.5, and 8.75, respectively (*5*). At pH 4.5, Arg426 is predominantly in the R conformation, remote from Tyr238, allowing the tyrosinate charge to delocalize onto the heme, enhancing oxoferryl formation and the peroxidase reaction (*26*). The equal proportions of Y and R at pH 6.5 suggest a facile equilibrium providing optimum conditions for both oxoferryl formation (conformation R) and oxoferryl reduction by H_2O_2 (conformation Y) required for the catalase reaction. At pH 8.5, Arg426 occupies predominantly conformation Y, associated with Tyr238, which inductively lowers electron density on the heme and adduct favoring perhydroxy-indole reduction in the oxidase reaction.

The properties of the R426K variant with the lysine side chain partially replacing the arginine in the catalase reaction but not in the oxidase reaction require some explanation. Modeling suggests that the lysine side chain at residue 428 cannot approach the Tyr238 tyrosinate ion as close as the arginine guanidinium without main chain distortion. This conclusion is consistent with the K426-Tyr238 interaction being too weak to facilitate perhydroxy-indole reduction, but it begs the question of how it is sufficiently strong to facilitate oxoferryl reduction in the catalase reaction. Several explanations are possible including the differences in structures of the oxoferryl and perhydroxy-indole structures, in their locations relative to K426-Tyr238, in the electron donors (H_2O_2 and NADH), in their binding locations, and possibly even in the ratio of Y and R conformations of the Lys426 side chain.

REFERENCES

1. Claiborne, W., and Fridovich, I. (1979) Purification of the *o*-dianisidine peroxidase from *Escherichia coli* B. Physicochemical characterization and analysis of its dual catalatic and peroxidatic activities, *J. Biol. Chem. 254*, 4245−4252.
2. Triggs-Raine, B. L., Doble, B. W., Mulvey, M. R., Sorby, P. A., and Loewen, P. C. (1988) Nucleotide sequence of *katG* encoding catalase HPI of *Escherichia coli*, *J. Bacteriol. 170*, 4415−4419.
3. Loewen, P. C., Triggs, B. L., George, C. S., and Hrabarchuk, B. E. (1985) Genetic mapping of *katG*, a locus that affects the synthesis of the bifunctional catalase-peroxidase HPI in *Escherichia coli*, *J. Bacteriol. 162*, 661−667.
4. Klotz, M. G., and Loewen, P. C. (2003) The molecular evolution of catalatic hydroperoxidases: Evidence for multiple lateral transfer of genes between prokaryota and from bacteria into eukaryota, *Mol. Biol. Evol. 20*, 1098−1112.

5. Singh, R., Wiseman, B., Deemagarn, T., Donald, L. J., Duckworth, H. W., Carpena, X., Fita, I., and Loewen, P. C. (2004) Catalase-peroxidases (KatG) exhibit NADH oxidase activity, *J. Biol. Chem. 279*, 43098−43106.
6. Zhang, Y., Heym, B., Allen, B., Young, D., and Cole, S. (1992) The catalase-peroxidase gene and isoniazid resistance of *Mycobacterium tuberculosis*, *Nature 358*, 591−593.
7. Rozwarski, D. A., Grant, G. A., Barton, D. H. R., Jacobs, W. R., and Sacchettini, J. C. (1998) Modification of the NADH of the isoniazid target (InhA) from *Mycobacterium tuberculosis*, *Science 279*, 98−102.
8. Lei, B., Wei, C. J., and Tu, S. C. (2000) Action mechanism of antitubercular isoniazid: Activation by *Mycobacterium tuberculosis* KatG, isolation and characterization of InhA inhibitor, *J. Biol. Chem. 275*, 2520−2526.
9. Wilming, M., and Johnsson, K. (1999) Spontaneous formation of the bioactive form of the tuberculosis drug isoniazid, *Angew. Chem., Int. Ed. 38*, 2588−2590.
10. Mdluli, K., Slayden, R. A., Zhu, Y., Ramaswamy, S., Pan, X., Mead, D., Crane, D. D., Musser, J. M., and Barry, C. E. (1998) Inhibition of a *Mycobacterium tuberculosis* β-ketoacyl ACP synthase by isoniazid, *Science 280*, 1607−1610.
11. Welinder, K. G. (1992) Superfamily of plant, fungal and bacterial peroxidases, *Curr. Opin. Struct. Biol. 2*, 388−393.
12. Ivancich, A., Jakopitsch, C., Auer, M., Un, S., and Obinger, C. (2003) Protein-based radicals in the catalase-peroxidase *Synechocystis* PCC6803: a multifrequency EPR investigation of wild-type and variants on the environment of the heme active site, *J. Am. Chem. Soc. 125*, 14093−14102.
13. Yamada, Y., Saijo, S., Sato, T., Igarashi, N., Usui, H., Fujiwara, T., and Tanaka, N. (2001) Crystallization and preliminary X-ray analysis of catalase-peroxidase from the halophilic archaeon *Haloarcula marismortui*, *Acta Crystallogr. D 57*, 1157−1158.
14. Yamada, Y., Fujiwara, T., Sato, T., Igarashi, N., and Tanaka, N. (2002) The 2.0 Å crystal structure of catalase-peroxidase from *Haloarcula marismortui*, *Nat. Struct. Biol. 9*, 691−695.
15. Donald, L. J., Krokhin, O. V., Duckworth, H. W., Wiseman, B., Deemagarn, T., Singh, R., Switala, J., Carpena, X., Fita, I., and Loewen, P. C. (2003) Characterization of the catalase-peroxidase KatG from *Burkholderia pseudomallei* by mass spectrometry, *Biol. Chem. 278*, 35687−35692.
16. Carpena, X., Loprasert, S., Mongkolsuk, S., Switala, J., Loewen, P. C., and Fita, I. (2003) Catalase-peroxidase KatG of *Burkholderia pseudomallei* at 1.7 Å resolution, *J. Mol. Biol. 327*, 475−489.
17. Wada, K., Tada, T., Nakamura, Y., Kinoshita, T., Tamoi, M., Sigeoka, S. and Nishimura, K. (2002) Crystallization and preliminary X-ray diffraction studies of catalase-peroxidase from *Synechococcus* PCC7492, *Acta Crystallogr. D 58*, 157−159.
18. Bertrand, T., Eady, N. A. J., Jones, J. N., Nagy, J. M., Jamart-Grégoire, B., Raven, E. L., and Brown, K. A. (2004) Crystal structure of *Mycobacterium tuberculosis* catalase-peroxidase, *J. Biol. Chem. 279*, 38991−38999.
19. Hillar, A., Peters, B., Pauls, R., Loboda, A., Zhang, H., Mauk, A. G., and Loewen, P. C. (2000) Modulation of the activities of catalase-peroxidase HPI of *Escherichia coli* by site-directed mutagenesis, *Biochemistry 39*, 5868−5875.
20. Regelsberger, G., Jakopitsch, C., Ruker, F., Krois, D., Peschek, G. A., and Obinger, C. (2000) Effect of distal cavity mutations on the formation of compound I in catalase-peroxidases, *J. Biol. Chem. 275*, 22854−22861.
21. Yu, S., Girotto, S., Zhao, X., and Magliozzo, R. S. (2003) Rapid formation of compound II and a tyrosyl radical in the Y229F mutant of *M. tuberculosis* KatG disrupts catalase but not peroxidase function, *J. Biol. Chem. 278*, 44121−44127.
22. Jakopitsch, C., Auer, M., Ivancich, A., Ruker, F., Furtmuller, P. G., and Obinger, C. (2003) Total conversion of bifunctional catalase-peroxidase (KatG) to monofunctional peroxidase by exchange of a conserved distal side tyrosine, *J. Biol. Chem. 278*, 20185−20191.
23. Jakopitsch, C., Ivancich, A., Schmuckenschlager, F., Wanasinghe, A., Pöltl, G., Furtmüller, P., Rükert, F., and Obinger, C. (2004) Influence of the unusual covalent adduct on the kinetics and formation of radical intermediates in *Synechocystis* catalase peroxidase, *J. Biol. Chem. 279*, 46082−46095.
24. Jakopitsch, C., Auer, M., Regelsberger, G., Jantschko, W., Furtmuller, P. G., Ruker, F., and Obinger, C. (2003) Distal site aspartate is essential in the catalase activity of catalase-peroxidases, *Biochemistry 42*, 5292−5300.
25. Jakopitsch, C., Auer, M., Regelsberger, G., Jantschko, W., Furtmuller, P. G. Ruker, F., and Obinger, C. (2003) The catalytic role of the distal site asparagine-histidine couple in catalase-peroxidases, *Eur. J. Biochem. 270*, 1006−1013.
26. Carpena, X., Wiseman, B., Deemagarn, T., Singh, R., Switala, J., Ivancich, A., Fita, I., and Loewen, P. C. (2005) A molecular switch and electronic circuit modulate catalase activity in catalase-peroxidases, *EMBO reports 6*, 1156−1162.
27. Carpena, X., Switala, J., Loprasert, S., Mongkolsuk, S., Fita, I., and Loewen, P. C. (2002) Crystallization and preliminary X-ray analysis of the catalase-peroxidase KatG from *Burkholderia pseudomallei*, *Acta Crystallogr. D 58*, 2184−2186.
28. Otwinowski, Z., and Minor, W. (1997) Processing of X-ray diffraction data collected in oscillation mode, *Methods Enzymol. 276*, 307−326.
29. Murshudov, G. N., Vagin, A. A., and Dodson, E. J. (1997) Refinement of macromolecular structures by the maximum-likelihood method, *Acta Crystallog. D 53*, 240−255.
30. Jones, T. A., Zou, J. Y., Cowan, S. W., and Kjeldgaard, M. (1991) Improved methods for building protein models in electron density maps, *Acta Crystallogr. A 47*, 110−119.
31. Evans, S. (1993) SETOR: Hardware lighted three-dimensional solid model representations of macromolecules, *J. Mol. Graphics 11*, 134−138.
32. Rorth, H. M., and Jensen, P. K. (1967) Determination of catalase activity by means of the Clark electrode, *Biochim. Biophys. Acta 139*, 171−173.
33. Childs, R. E., and Bardsley, W. G. (1975) The steady-state kinetics of peroxidase with 2,20-azino-di-(3-ethyl-benzthiazoline-6-sulphonic acid) as chromagen, *Biochem. J. 145*, 93−103
34. Layne, E. (1957) Spectrophotometric and turbidimetric methods for measuring proteins, *Methods Enzymol. 3*, 447−454.
35. Deemagarn, T., Carpena, X., Singh, R., Wiseman, B., Fita, I., and Loewen, P. C. (2005) Structural characterization of the Ser324Thr variant of the catalase-peroxidase (KatG) from *Burkholderia pseudomallei*, *J. Mol. Biol. 345*, 21−28.
36. Hirst, J., Wilcox, S. K., Williams, P. A., Blankenship, J., McRee, D. E., and Goodin, D. B. (2001) Replacement of the axial histidine ligand with imidazole in cytochrome *c* peroxidase. 1. Effects on structure, *Biochemistry 40*, 1265−1273.
37. Hirst, J., Wilcox, S. K., Ai, J., Moenne-Loccoz, P., Loehr, T. M., and Goodin, D. B. (2001) Replacement of the axial histidine ligand with imidazole in cytochrome *c* peroxidase. 2. Effects on heme coordination and function, *Biochemistry 40*, 1274−1283.

BI060017F